




Activation of the ILT7 receptor and plasmacytoid dendritic cell responses are governed by structurally-distinct BST2 determinants

Received for publication, March 15, 2019, and in revised form, April 25, 2019. Published, Papers in Press, May 22, 2019, DOI 10.1074/jbc.RA119.008481

 Mariana G. Bego[‡], Nolwenn Miguet[§], Alexandre Laliberté[‡], Nicolas Aschman[§], Francine Gerard[§], Angelique A. Merakos[‡],  Winfried Weissenhorn[§], and  Éric A. Cohen^{‡¶1}

From the [‡]Institut de Recherches Cliniques de Montréal, Montreal, Quebec H2W 1R7, Canada, the [§]University Grenoble Alpes, Institut de Biologie Structurale (IBS), CEA, CNRS, 38044 Grenoble, France, and the [¶]Department of Microbiology, Infectiology and Immunology, Université de Montréal, Montreal, Quebec H3T 1J4, Canada

Edited by Charles E. Samuel

Type I interferons (IFN-I) are key innate immune effectors predominantly produced by activated plasmacytoid dendritic cells (pDCs). By modulating immune responses at their foundation, IFNs can widely reshape immunity to control infectious diseases and malignancies. Nevertheless, their biological activities can also be detrimental to surrounding healthy cells, as prolonged IFN-I signaling is associated with excessive inflammation and immune dysfunction. The interaction of the human pDC receptor immunoglobulin-like transcript 7 (ILT7) with its IFN-I-regulated ligand, bone marrow stromal cell antigen 2 (BST2) plays a key role in controlling the IFN-I amounts produced by pDCs in response to Toll-like receptor (TLR) activation. However, the structural determinants and molecular features of BST2 that govern ILT7 engagement and activation are largely undefined. Using two functional assays to measure BST2-stimulated ILT7 activation as well as biophysical studies, here we identified two structurally-distinct regions of the BST2 ectodomain that play divergent roles during ILT7 activation. We found that although the coiled-coil region contains a newly defined ILT7-binding surface, the N-terminal region appears to suppress ILT7 activation. We further show that a stable BST2 homodimer binds to ILT7, but post-binding events associated with the unique BST2 coiled-coil plasticity are required to trigger receptor signaling. Hence, BST2 with an unstable or a rigid coiled-coil fails to activate ILT7, whereas substitutions in its N-terminal region enhance activation. Importantly, the biological relevance of these newly defined domains of BST2 is underscored by the identification of substitutions having opposing potentials to activate ILT7 in pathological malignant conditions.

Type I interferons (IFN-I)² are key soluble antiviral molecules that are predominantly produced by activated plasmacytoid dendritic cells (pDCs) (1). Their functions reach far beyond their established role during antimicrobial defense as IFN-I are also linked with regulation of immune cell differentiation, survival, and homeostasis as well as control of the cell cycle (2–4). Hence, IFN-I play an important role in orchestrating the natural immune response to cancer and have inhibitory functions that prevent malignant cellular transformation (reviewed in Zitvogel *et al.* (5)). However, their biological activities can also have deleterious impacts on surrounding healthy cells. Prolonged IFN-I signaling is associated to excessive inflammation and immune dysfunction (6) and high levels of IFN-I contributes to aberrant immune activation and development of autoimmune diseases (7). Furthermore, IFN-I's can also act as a double-edged sword when fighting malignant invasive tumors, with the potential to deploy opposite anti- and pro-tumorigenic outcomes given their direct impact on tumor cells and potentially improper activity on tumor infiltrating immune cells (8). Thus, IFN-I production and signaling need to be tightly regulated to achieve protective immunity during pathological conditions while avoiding harmful toxicity caused by improper or prolonged IFN signaling.

One way to control IFN-I production involves the engagement of pDC-specific regulatory receptors BDCA-2 (CD303) and ILT7 (LILRA4, CD85g). Cross-linking of either regulatory receptor efficiently suppresses the production of IFN-I and other cytokines in response to Toll-like receptors 7 and 9 (TLR7/9) activation (9, 10). Interestingly, the natural ligand of ILT7 was found to be BST2, a membrane-associated protein that is itself induced by IFN-I (11). Given the IFN-I-inducible nature of the ILT7 ligand, it was proposed that BST2 contributes to a negative feedback mechanism controlling IFN-I overproduction by pDCs after viral infection and/or sustained

This work was supported by Canadian Institutes of Health Research (CIHR) Grants PJT148686 and FDN 154324 and an IRCM-UdeM Chair of Excellence in HIV research (to É. A. C.), ANRS Grant 073744 (to W. W.), the Institute Universitaire de France (IUF) and Grenoble Partnership for Structural Biology platforms (ISBG) UMS 3518 CNRS-CEA-UJF-EMBL funded by FRISBI (ANR-10-INSB-05-02) and GRAL (ANR-10-LABX-49-01). This work was also supported by a Ph.D. fellowship from the Fond National de la Recherche Luxembourg (to N. A.). The authors declare that they have no conflicts of interest with the contents of this article.

This article contains Tables S1–S2 and Figs. S1–S5.

¹ To whom correspondence should be addressed: Laboratory of Human Retrovirology, Institut de Recherches Cliniques de Montréal, 110 Pine Ave. West, Montreal, Quebec H2W 1R7, Canada. Tel.: 514-987-5804; Fax: 514-987-5691; E-mail: eric.cohen@ircm.qc.ca.

² The abbreviations used are: IFN-I, type I interferons; BST2, bone marrow stromal cell antigen 2; GST, glutathione S-transferase; GPI, glycosylphosphatidylinositol; ILT7, immunoglobulin-like transcript 7; MFI, mean fluorescence intensity; MST, microscale thermophoresis; pDCs, plasmacytoid dendritic cells; SNP, single nucleotide polymorphisms; SPR, surface plasmon resonance; TLR, Toll-like receptor; HEK, human embryonic kidney; RU, response unit; PBMC, peripheral blood mononuclear cell; NFAT, nuclear factor of activated T cells; ANOVA, analysis of variance.

Distinct domains of BST2 are involved in ILT7 activation

inflammatory responses (11–14). Remarkably, BST2 expression is constitutively elevated in various cancers such as myelomas, lung cancer, breast cancer, colorectal cancer, and pancreatic cancer (15). Indeed, constitutive expression of BST2 by human breast cancer cell and melanoma lines was shown to suppress IFN-I production by pDC via ILT7, raising the possibility that the interaction of BST2 with ILT7 *in trans* might be contributing to tumor immune suppression and pDC–tumor cross-talk (14).

BST2 is a small, evolutionary conserved, single-pass type II membrane protein. It has a unique topology as its ectodomain is anchored to the plasma membrane via a N-terminal transmembrane domain and a C-terminal glycosylphosphatidylinositol (GPI) anchor (16) (Fig. 1A). BST2 contains a short cytoplasmic tail involved in NF- κ B signaling and AP-2–dependent endocytosis (17, 18). The protein is heavily glycosylated on two conserved extracellular asparagine residues (Asn-65 and Asn-92) and forms a stable disulfide-linked dimer via any of the three conserved cysteine residues located toward the N-terminal region of the ectodomain (Cys-53, Cys-63, and Cys-91) (16, 19–22).

The structure of the human and mouse BST2 ectodomain dimers have been solved by X-ray crystallography. Each monomer consists of a continuous α helix organized in parallel orientation, forming a homodimer with a coiled-coil structure stabilized by intermolecular disulfide linkages (23–26). Biophysical studies indicate that the recombinant coiled-coil BST2 ectodomain dimer exists as a rod-like structure of 15 to 17 nm in length with a slight bend at about one-third from its N terminus (26, 27). The ectodomain dimer is hinged at two positions (Ala-88 and Gly-109 in the human protein), giving the N terminus a degree of rotational flexibility (24–26). In both species, the ectodomain two-thirds C-terminal region is arranged as a parallel dimeric coiled-coil formed by 6–7 heptad repeats starting at position Cys-91 (23–26). The presence of a number of destabilizing residues in key central heptad positions confer the ectodomain coiled-coil its characteristic dynamic instability that requires intermolecular disulfides for stability (23). Such an evolutionary conserved design was proposed to provide the BST2 dimer an inherent plasticity that allows the protein to adapt during dynamic events (23, 27).

BST2 is a multifaceted protein. It is also referred as “tetherin,” as it acts as a broad antiviral restriction factor through its ability to physically retain enveloped viruses at the cell surface, thus preventing their release from infected cells (28, 29). We recently reported that while “tethering” HIV type 1 (HIV-1), BST2 is unable to interact with ILT7 and block IFN-I production by pDCs (30). Remarkably, the pandemic HIV-1 group M has evolved mechanisms to maintain BST2–ILT7 interaction and limit pDC activation despite its ability to effectively counteract BST2 for efficient HIV-1 release (30). This property, which limits pDC antiviral responses, was not conserved in the endemic HIV-1 group O (30, 31). Although the domains and structural features of BST2 required for tethering HIV-1 have been precisely defined (22, 23, 28, 32, 33), the determinants required for engaging and activating ILT7 are largely undefined. Understanding the structural features of BST2 that are required to engage and activate ILT7 may guide the develop-

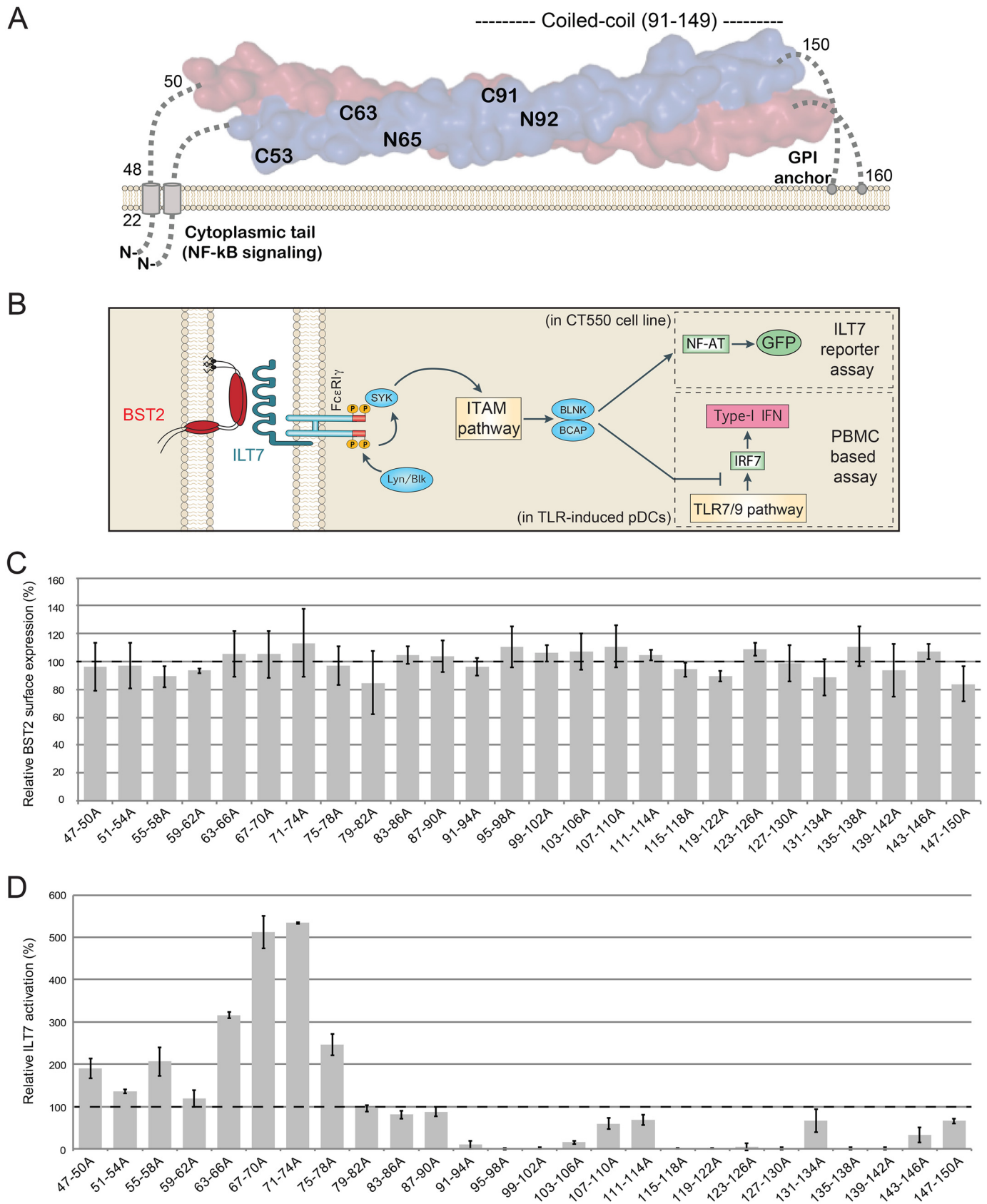
ment of new therapeutic options aimed at restoring pDC functionality and triggering IFN-I production to induce effective antitumor or antiviral immunity.

Using functional assays measuring ILT7 activation by BST2 as well as biophysical studies of BST2 interaction with ILT7, we show that the structurally distinct N- and C-terminal regions of BST2 ectodomain have discrete functions during ILT7 activation. Although the unique and highly conserved C-terminal coiled-coil region of BST2 contains key residues required for ILT7 binding, the N-terminal and its central connecting flexible region acts as a modulatory region suppressing ILT7 activation. Indeed, we provide evidence that after the initial interaction, the coiled-coil internal flexibility is required for ILT7 activation suggesting a post-binding conformational rearrangement of the BST2/ILT7 complex. We further demonstrate that a stable BST2 homodimer is required to trigger ILT7 activation and that both BST2 monomers need to have an intact ILT7-binding surface for this function. Importantly, analysis of somatic mutations identified in particular tumor tissues and mapping to these newly defined BST2 functional domains reveals that specific genetic changes in BST2 are capable of either greatly enhancing ILT7-mediated suppression of IFN-I production or completely abrogating this phenotype, thus underscoring the clinical relevance of our findings.

Results

The highly conserved coiled-coil region of BST2 is required for ILT7 activation

We previously demonstrated that the BST2 ectodomain is sufficient to interact with ILT7 and activate its inhibitory signaling cascade (30). To identify the determinants in BST2 ectodomain required for ILT7 activation we used two previously described co-culture assays, namely a reconstituted ILT7 reporter assay and a PBMC-based assay (Fig. 1B). The first functional assay relies on a mouse NFAT-GFP reporter cell line, which also expresses human ILT7 and the mouse Fc ϵ RI γ chain (CT550) such that levels of GFP expression directly correlates with the degree of BST2-mediated ILT7 activation (10, 11). Selected BST2 mutants were also tested in a PBMC-based co-culture assay, which directly measures the quantity of IFN-I produced by PBMCs after TLR7 agonist stimulation following engagement and activation of the ILT7 pathway in pDCs by BST2 (30, 34). Given that the extent of ILT7 activation is directly proportional to the surface levels of BST2 expressed on co-cultured 293T targets cells (30), expression of all BST2 mutants was standardized to match that of the internal BST2 WT control (Fig. S1). A series of alanine substitutions starting at amino acid position 47 and continuing through position 150 (32), where each mutant in the panel incorporates four consecutive alanine residues, was used to identify determinants required for ILT7 activation. HEK-293T cells expressing BST2 (WT or mutants) were co-cultured with ILT7⁺ NFAT-GFP reporter cells prior to flow cytometry analysis. The alanine scan analysis revealed two discrete domains in BST2 that modulate ILT7 activation. A first region spanning residues 47 to 90 appeared to act as a modulatory domain as alanine substitutions enhanced BST2-mediated ILT7 activation. In contrast, a



Distinct domains of BST2 are involved in ILT7 activation

second region overlapping the BST2 coiled-coil domain from residues 91 to 147 seemed to have a direct role in ILT7 activation as many alanine substitutions resulted in a strong impairment of the ILT7 activation phenotype (Fig. 1, C and D).

A surface required for ILT7 activation is defined by two spatially adjacent residues within the BST2 coiled-coil

We confirmed that the BST2 coiled-coil region was sufficient to interact with ILT7 by surface plasmon resonance *in vitro* ($K_D = 2.22 \mu\text{M}$) using recombinant GST-tagged truncated BST2 (residues 80 to 147) and baculovirus-expressed soluble ILT7 (Fig. 2A). The primary structure of the coiled-coils is characterized by a periodicity of seven residues or heptad repeat pattern, which are usually labeled *abcdefg*. Heptad positions *a* and *d* (typically hydrophobic residues) form the core present at the interface of the two helices, whereas *e* and *g* positions (typically charged residues) form inter-helical ionic interactions and are all involved in dimer stabilization (35, 36). Some of the alanine residues introduced during the alanine scan could potentially disrupt the stability of the coiled-coil structure, especially those that substitute amino acid residues located at the center of the α -helix (heptad positions *a* and *d*) or those involved in stabilizing inter-helical bonds (heptad positions *e* and *g*; Fig. 2, B and C). Furthermore, as the BST2 ectodomain parallel dimer is anchored to the plasma membrane at both ends, at least one of heptad positions *e* or *g* is most probably buried as it is facing the cell surface (Fig. 2C). We therefore reasoned that only heptad positions *b*, *c*, and *f* are more likely to be exposed for interaction with ILT7. Based on these predictions, we selected potentially exposed nonalanine residues, which were part of the quadruple alanine scan null mutants, for individual studies (Fig. 2, B and C). Several mutations had a slight to severe ILT7 activation phenotype impairment, but two BST2 mutants, D129A and R136A, completely lost their ability to activate ILT7 (Fig. 3, A and B). The defective phenotype of BST2 D129A and R136A mutants was confirmed using the PBMC-based assay. As expected, upon engagement of BST2 WT with ILT7, IFN-I production was significantly reduced in the co-culture (Fig. 3C and Fig. S2). In agreement with the lack of ILT7 activation observed using the ILT7 reporter assay, BST2 D129A and R136A mutants were unable to significantly trigger a repression of the IFN-I pathway triggered through TLR7 activation (Fig. 3C and Fig. S2). Interestingly, the two mutated residues Asp-129 and Arg-136 are located in adjacent *c* heptad positions (Fig. 2C) and as such could form a potential

ILT7-binding surface in the secondary structure of BST2 (Fig. 3D).

BST2 coiled-coil dynamic instability is important to modulate ILT7 activation

Alanine substitutions of residues 63 to 78 in the N-terminal region of the BST2 ectodomain enhanced ILT7 activation by 3- to 5-fold (Fig. 1D). This same region was previously shown to display pronounced flexibility in the context of BST2 dimers and to act as the core of a putative antiparallel 4-helix bundle made by two BST2 parallel dimers under reducing conditions (24, 25). A single residue substitution in this region, L70D, was sufficient to disrupt tetramers without affecting the formation of BST2 dimers under reducing conditions, but had only limited effects on BST2 antiviral activity (24). When tested in the ILT7 reporter assay, substitution of leucine at position 70 for aspartic acid significantly enhanced activation (Fig. 4, A and B). Interestingly, this mutant behaved just as BST2 WT in the PBMC-based assay (Fig. 4C). Given the structural feature displayed by this region, the L70D substitution could also have long range effects on the dynamic of the coiled-coil region. Crystal structure models from Schubert and colleagues (24) suggest that residue Leu-70 is buried in a hydrophobic core stabilizing the BST2 dimer. It is therefore possible that disrupting a strong hydrophobic core within the N terminus end of the dimer by adding a charged residue would provide more flexibility to the C terminus coiled-coil domain. To test whether the dynamic instability of the BST2 coiled-coil plays a role in ILT7 activation, we incorporated two cysteines at positions Leu-127 (L127C) and Val-134 (V134C) predicted to be close enough in the dimer to allow formation of disulfide bonds (Fig. 4D). As predicted, restricting the plasticity of the BST2 coiled-coil region significantly reduced ILT7 activation in the ILT7 reporter assay as well as in the PBMC-based assay (Fig. 4, A–C). These results highlight the importance of the BST2 coiled-coil characteristic of dynamic instability for ILT7 activation and suggest that the N-terminal region of the BST2 ectodomain might impose a structural constraint on the coiled-coil dynamic.

ILT7 activation requires a structurally stable BST2 dimer

Although there are three disulfide bonds (Cys-53, Cys-63, and Cys-91) stabilizing the BST2 dimer (24–26), none of the three individually is required for BST2 antiviral function (21, 22). Loss of cysteines at position 53 and 63 did not affect the

Figure 1. Uncovering BST2 regions relevant for ILT7 activation using an alanine scan analysis of its ectodomain. A, schematic representation of BST2, a type II transmembrane (TM) protein of 160 amino acids, overlaying the crystal structure of BST2 ectodomain (PDB code 2XG7) published by Schubert *et al.* (24) generated using NGL viewer (46). BST2 features a short cytoplasmic N terminus containing diphosphotyrosines required for NF- κ B signaling followed by an α -helical single-pass TM domain and an ectodomain comprising an extended coiled-coil linked back to the plasma membrane by a C-terminal GPI anchor. N-Glycosylation sites (Asn-65 and Asn-92) as well as cysteine residues used for disulfide-bond formation (Cys-53, Cys-63, and Cys-91) in the extracellular domain are indicated. B, schematic representation of BST2–ILT7 activation pathways and the two assays used to measure BST2-mediated ILT7 activation. For the ILT7 reporter assay, BST2-expressing HEK-293T cells are co-cultured with ILT7⁺ NFAT-GFP reporter cells for 18–24 h and activation of the ITAM pathways measured as the percentage of GFP⁺ reporter cells by flow cytometry. For the PBMC-based assay, BST2-expressing HEK-293T cells were co-cultured with PBMCs. After 4 h of co-culture, samples were either untreated or treated with Gardiquimod (TLR7 agonist) and levels of bioactive IFN-I released in supernatants measured 18–24 h later, as described under “Experimental procedures.” C and D, alanine scan of the BST2 ectodomain (nonoverlapping groups of 4 residues substituted to alanines from positions 47 to 150). C, relative BST2 surface expression in HEK-293T cells transfected with empty plasmid, plasmid encoding for BST2 WT or alanine mutants ($n = 6$). Percentages of MFIs were calculated relative to BST2 WT-expressing cells (100%). D, ILT7⁺ NFAT-GFP reporter cells were co-cultured with control (empty) or HEK-293T cells expressing the above-mentioned BST2 (WT or mutants, shown in C) and analyzed by flow cytometry ($n = 6$). Percentage of ILT7 activation was plotted as % of GFP⁺ cells in each condition relative to the BST2 WT condition (100%) after subtracting the % of GFP⁺ cells in the no BST2 condition (0%). Error bars represent S.D. Amino acids are represented as single letter codes in the figure.

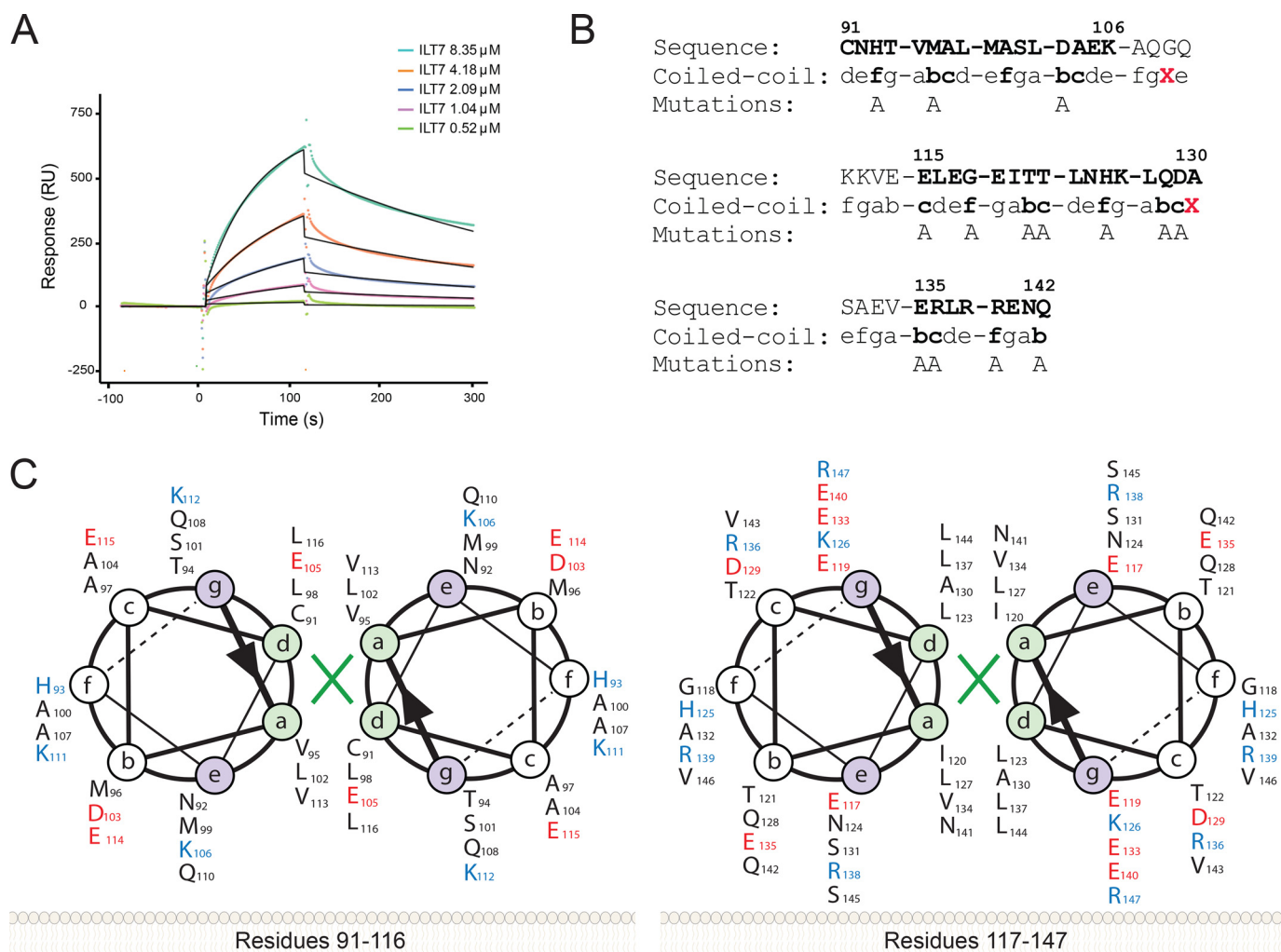


Figure 2. Binding of ILT7 to BST2 coiled-coil region. A, recombinant GST-BST2(80–147) pre-coated on the surface of Biacore sensor chip, was mixed with the indicated concentrations of bacILT7(24–435). The kinetic response data after subtracting the value from a reference cell coated with GST alone are shown. Kinetic constants ($K_D = 2.22 \mu\text{M}$, $k_{on} = 1.27 \times 10^3 \text{ M}^{-1} \text{ s}^{-1}$, $k_{off} = 2.81 \times 10^{-3} \text{ s}^{-1}$) were derived by global fitting the data corresponding to the five indicated concentrations (dotted lines) to a 1:1 Langmuir model (black lines) using local R_{max} parameters ($\chi^2 = 10.2$). B, identification of potentially individual exposed residues within the BST2 coiled-coil region. Sequence of BST2 coiled-coil region, position of alanine mutations that failed to activate ILT7 (in **bold**), coiled-coil heptad positions (denoted a–g), positions most likely to be exposed (in **bold**; stutter position in **red**), as well as individual alanine substitutions of predicted BST2 exposed residues are indicated. C, helical wheel diagram of the homodimeric parallel coiled-coil of BST2 (residues depicted from positions 91–116 and 117–147). The primary structure of each helix is characterized by a periodicity of seven residues or heptad repeat pattern. Heptad positions a and d (shaded green) are typically hydrophobic core residues present at the interface of the two helices, whereas e and g positions (shaded purple) typically form inter-helical ionic interactions and are all involved in the dimer formation. Residues often found in the remaining heptad repeat positions b, c, and f are exposed for potential interaction with binding partners. Charged amino acids are colored (negative in red and positive in blue). Given the BST2 unique double membrane anchored conformation, its fixed membrane facing interphase is highlighted as well. Amino acids are represented as single letter codes in the figure.

ability of BST2 to activate ILT7 (Fig. 5, A and B). On the other hand, loss of cysteine residue at position 91 drastically reduced ILT7 activation. Indeed, any combination that included a mutation at cysteine 91 displayed a strong defect in ILT7 activation (Fig. 5, A and B). Of note, GlcNAc residues at Asn-92 are postulated to be perpendicular to the Cys-91–Cys-91 disulfide bond (24). Interestingly, whereas N-glycosylation sites were not required for ILT7 activation, disrupting Cys-91 disulfide bond in the absence of glycosylation at position 92 restored BST2-mediated ILT7 activation to BST2 WT levels (Fig. 5, A and B). Nevertheless, the stabilizing role of the disulfide bonds was found to be required for ILT7 activation as substitution N92Q could not rescue activation when the three cysteines were replaced (Fig. 5, A and B). In agreement with the ILT7 reporter cell assay, the BST2 C91A mutant was unable to significantly

trigger the ILT7-dependent IFN-I repression pathway in PBMCs, whereas no significant differences were observed between BST2 WT and the C91A/N92Q mutant (Fig. 5C). These results indicate that although the structural stability of the BST2 dimer conferred by the disulfide bonds is critical for BST2-mediated ILT7 activation, the disulfide bond specifically formed through Cys-91 might also contribute to the proper orientation of a neighboring highly glycosylated site that otherwise could impair BST2–ILT7 engagement.

Given that a stable BST2 dimer is required to activate ILT7 and that the ILT7 co-receptor, FcεRIγ, requires dimerization for proper activation (37), we investigated whether ILT7 activation requires the engagement of two functionally active units within the BST2 dimer. Using a double inverse gradient of expression of BST2 WT *versus* the R136A null mutant, we

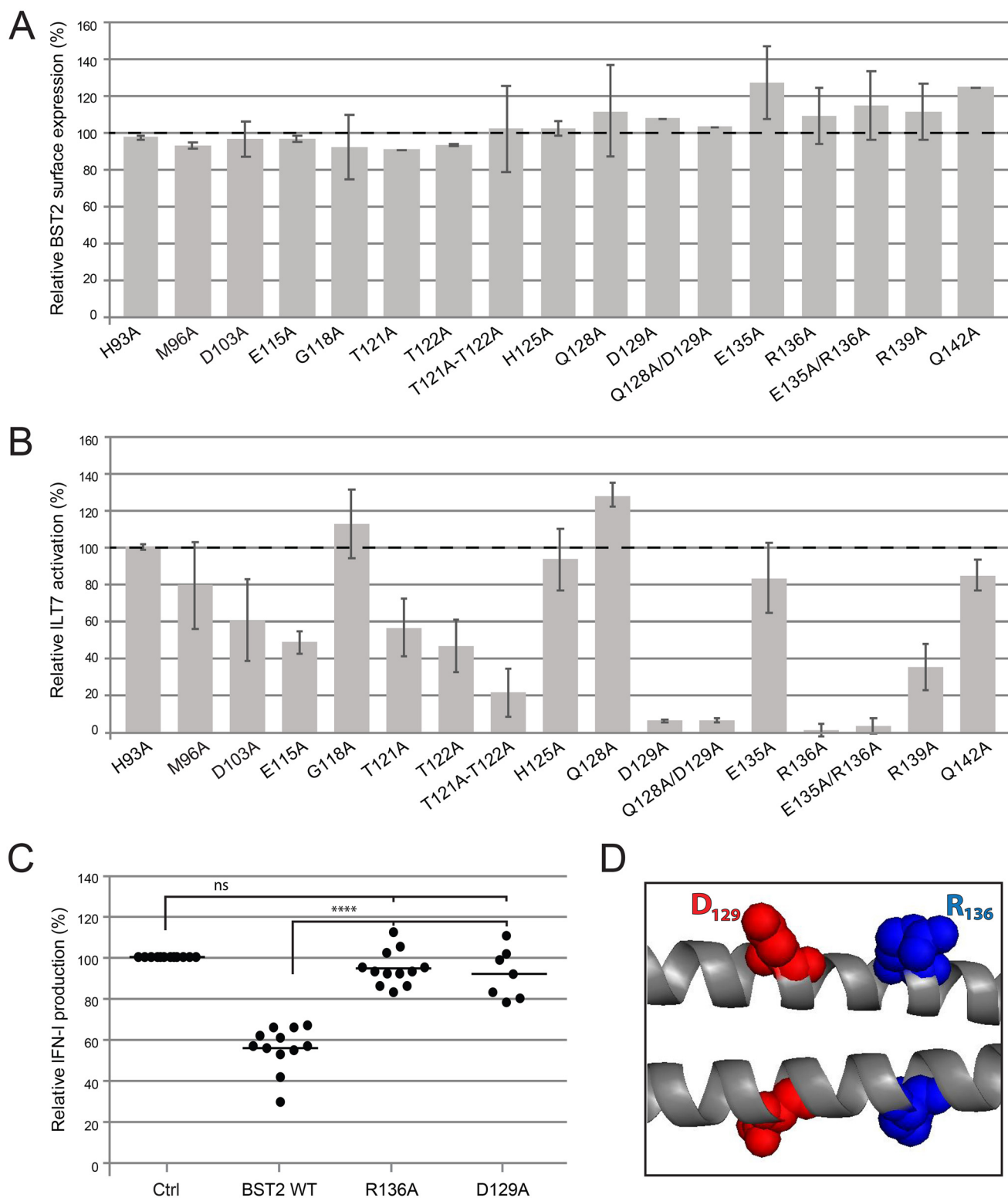


Figure 3. Effect of alanine substitutions of predicted exposed BST2 residues on ILT7 activation. *A*, relative BST2 surface expression in HEK-293T cells transfected with control plasmids or plasmids encoding the indicated BST2 mutants ($n = 6$). Percentages of MFIs were calculated as described in the legend to Fig. 1. *B*, ILT7⁺ NFAT-GFP reporter cells were co-cultured for 18–24 h with HEK-293T cells expressing the indicated BST2 mutants and analyzed by flow cytometry ($n = 6$). Percentage of ILT7 activation was plotted as described in the legend to Fig. 1. Error bars represent S.D. *C*, HEK-293T cells expressing the indicated BST2 mutants were co-cultured with freshly isolated PBMCs and levels of bioactive IFN-I released in supernatants in response to TLR7 agonist was measured 18–24 h later. Results are expressed as relative percentage of IFN-I released by PBMCs in contact with HEK-293T cells transfected with empty plasmid in the presence of TLR7 agonist (100%, $n = 12$). Statistical significance was determined by applying repeated measures ANOVA with Bonferroni's multiple comparison test. *D*, putative orientation of residues D129A and R136A extrapolated from the crystal structure of BST2 residues 80–147 published by Hinz *et al.* (26). Amino acids are represented as single letter codes in the figure.

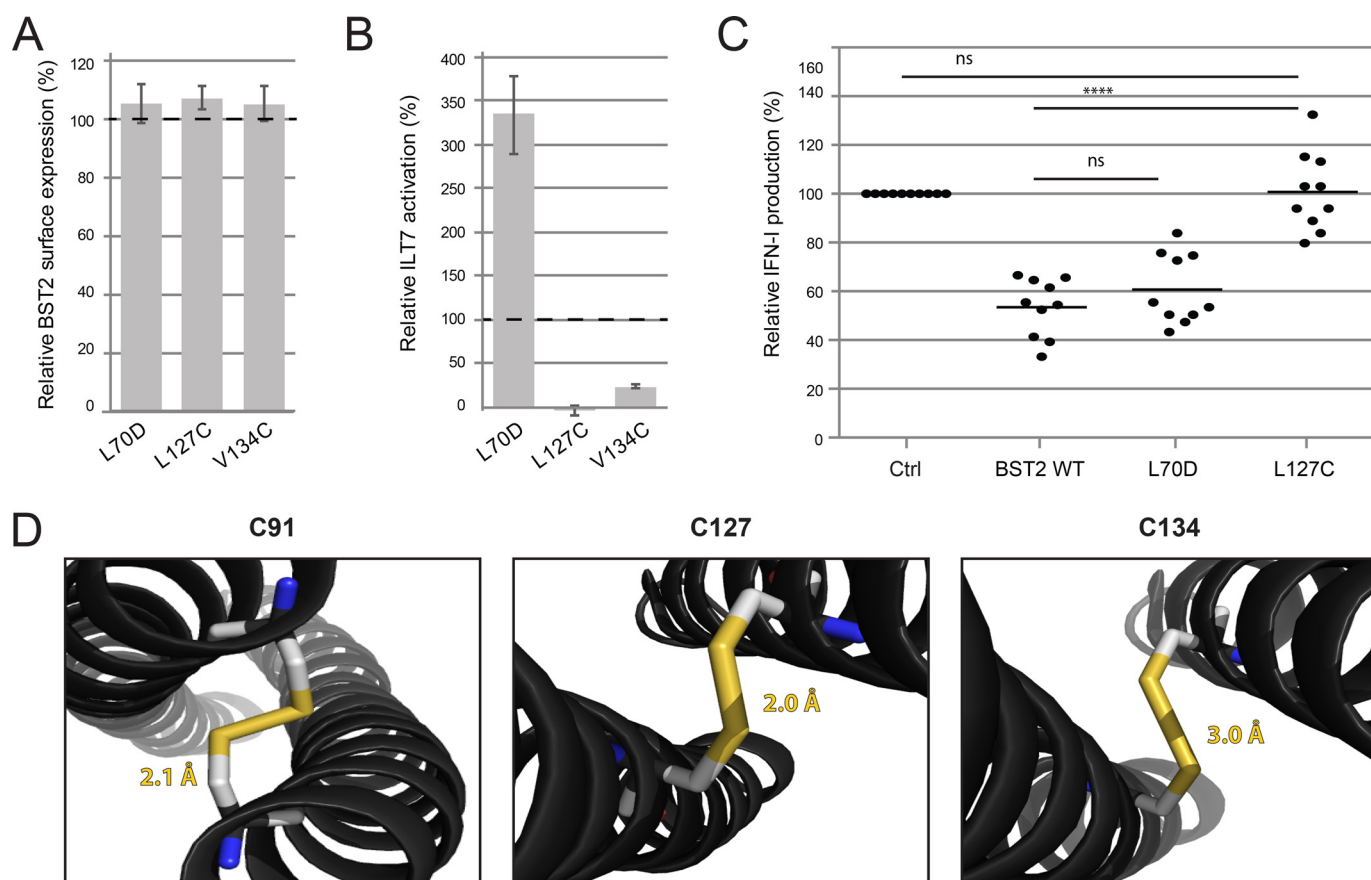


Figure 4. Effect of BST2 L70D mutation and incorporation of engineered disulfide bonds on ILT7 activation. A, relative BST2 surface expression in HEK-293T cells transfected with control plasmids or plasmids encoding the indicated BST2 mutants ($n = 6$). Percentages of MFIs were calculated as described in the legend to Fig. 1. B, ILT7⁺ NFAT-GFP reporter cells were co-cultured for 18–24 h with HEK-293T cells expressing the indicated BST2 mutants and analyzed by flow cytometry ($n = 6$). Percentage of ILT7 activation was plotted as described in the legend to Fig. 1. Error bars represent S.D. C, control, BST2 WT, or selected mutants (L70D and L127C) expressing HEK-293T cells were co-cultured with freshly isolated PBMCs and levels of bioactive IFN-1 released in supernatants in response to TLR7 agonist was measured as described in the legend to Fig. 3 ($n = 10$). D, predicted distance between natural cysteine at position 91 on sister BST2 helices as well as between cysteines replacing proposed polar dimerization contacts at positions 127 and 134 (in adjacent heptad positions, see Fig. 2, B and C). Cysteine replacements were introduced using Coot and disulfide bonds visualized using PyMOL. Distances were extrapolated from the crystal structure of BST2 residues 80–147 published by Hinz *et al.* (26). The distance between the sulfurs in the disulfide bond in Å is shown for each of the above-mentioned positions. Amino acids are represented as single letter codes in the figure.

determined that only homodimers of BST2 WT are capable of activating ILT7, whereas heterodimers between BST2 WT and the R136A mutant are inactive (Fig. 6, A and B, Fig. S3A). To support these findings, we demonstrated by co-immunoprecipitation assay that BST2 WT was capable of forming dimers with BST2 R136A as efficiently as with BST2 WT (Fig. S3B). These findings indicate that two functionally active units of BST2 forming a stable dimer are required to activate ILT7.

Natural variants of BST2 exhibit distinct ILT7 activation phenotypes

To examine if the BST2 functional domains identified so far can be affected *in vivo*, several natural variants of BST2 were analyzed, including SNPs and somatic mutations associated to specific cancers (Fig. 7A, Table S1). Most of the SNP tested were comparable with BST2 WT for ILT7 activation; however, three SNPs, namely D103N, E117A, and D129E, the latter revealing a substitution at the critical Asp-129 residue for a conserved charged amino acid, exhibited a partially impaired ILT7 activation phenotype (Fig. 7B). Likewise, three of the somatic muta-

tions tested (E62G, hepatocellular carcinoma; Q110H, ovarian cancer; and S145R, lung cancer) activated ILT7 to the same extent as BST2 WT. Interestingly, one somatic mutation (E119K, melanoma) located in the coiled-coil domain was completely defective, whereas three somatic mutations identified in distinct cancer tissues (C63Y, uterine cancer; Q87H, colon cancer; and T90P, breast cancer) and mapping outside of the coiled-coil structure exhibited enhanced activation capacities (Fig. 7B). In agreement with the ILT7 reporter assay, mutation E119K was completely defective in the PBMC assay (Fig. 7C). Based on its heptad *g* position (Fig. 2C), it is predicted that the charge alteration at this position would have a very detrimental effect on the overall coiled-coil stability, further highlighting the importance of the integrity of this structure for ILT7 activation. However, in contrast to the BST2 C63Y and T90P mutants that behaved just as WT in this assay, BST2 Q87H strongly repressed IFN-1 production (Fig. 7, B and C). Taken together these results suggest that variants of BST2 with opposing potential to activate ILT7 can be found *in vivo* under pathological malignant conditions.

Distinct domains of BST2 are involved in ILT7 activation

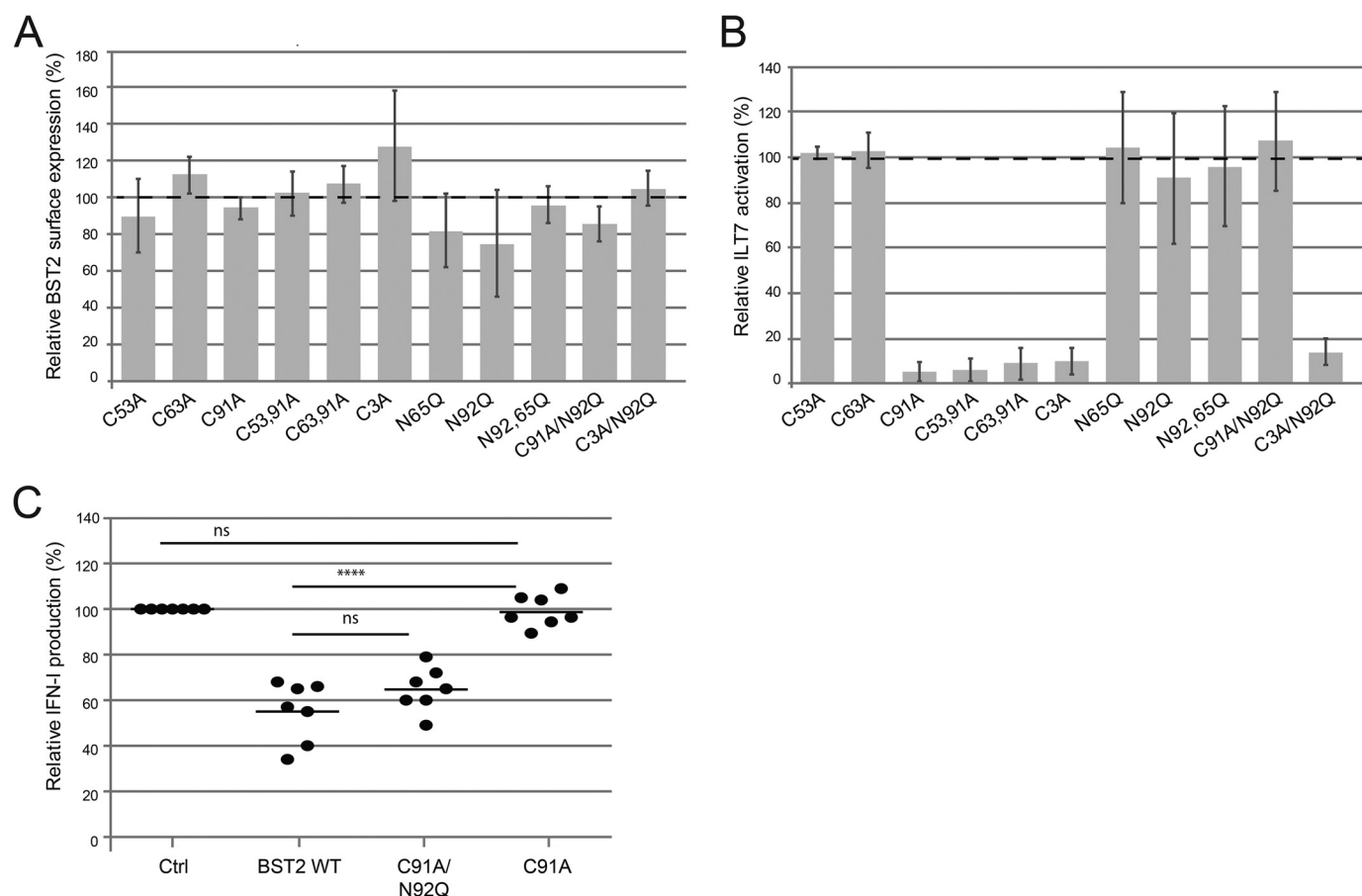


Figure 5. Role of BST2 cysteine or asparagine residues in ILT7 activation. A, relative BST2 surface expression in HEK-293T cells transfected with control plasmids or plasmids encoding the indicated BST2 variants ($n = 6$). Percentages of MFIs were calculated as described in the legend to Fig. 1. B, ILT7⁺ NFAT-GFP reporter cells were co-cultured for 18–24 h with HEK-293T cells expressing the indicated BST2 variants and analyzed by flow cytometry ($n = 6$). Percentage of ILT7 activation was plotted as described in the legend to Fig. 1. Error bars represent S.D. C, control, BST2 WT, or selected variants expressing HEK-293T cells were co-cultured with freshly isolated PBMCs and levels of bioactive IFN-γ released in supernatants in response to TLR7 agonist was measured as described in the legend to Fig. 3 ($n = 7$).

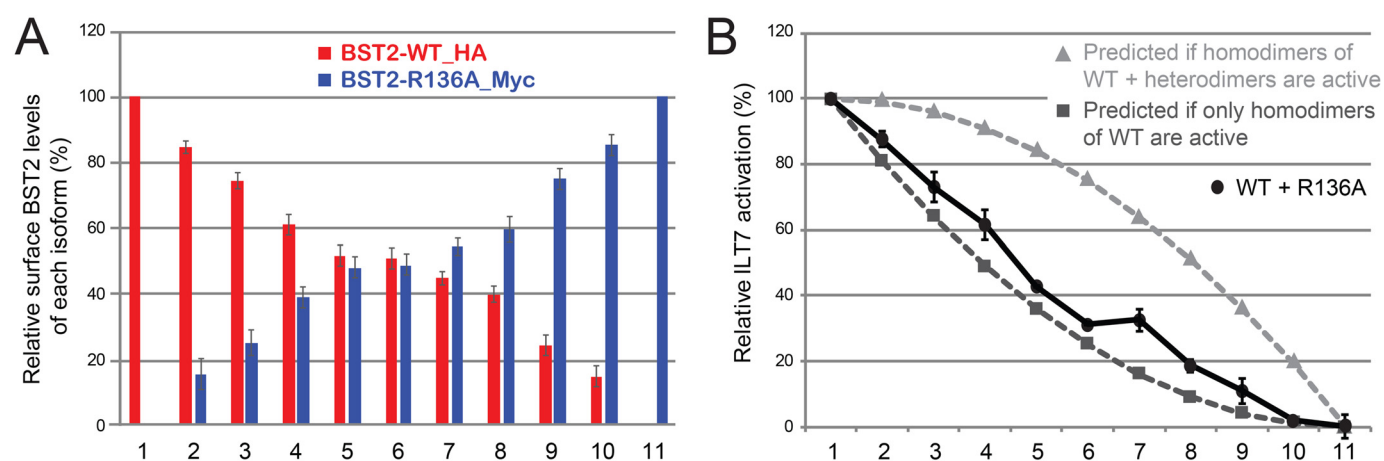
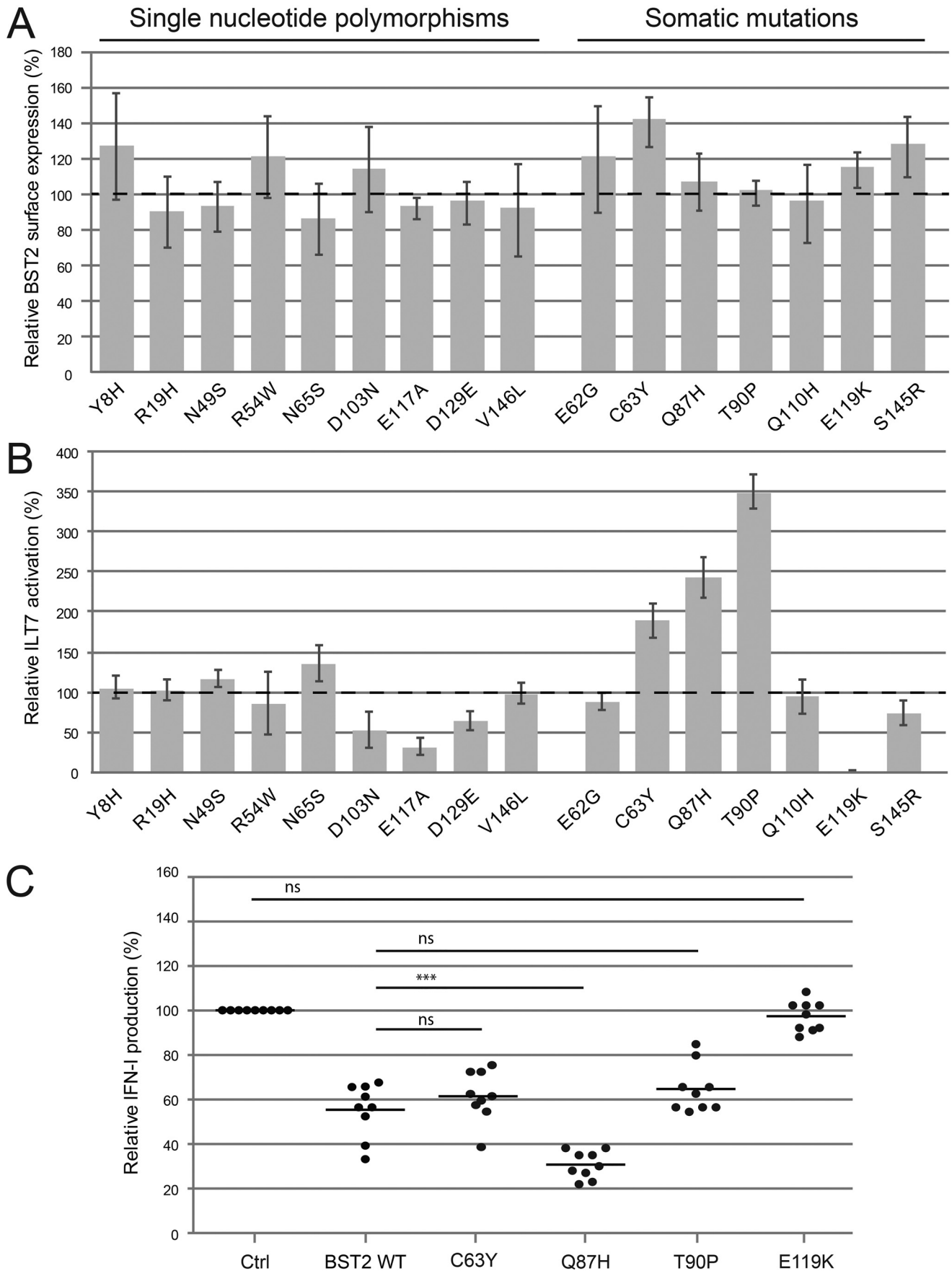


Figure 6. ILT7 activation in response to different ratios of functional and nonfunctional BST2 isoforms. A converging (or double) gradient of expression of HA-BST2 WT and Myc-BST2 R136A was generated in HEK-293T cells such that conditions 1 and 11 represent solely HA-BST2 WT or Myc-BST2 R136A, respectively, whereas condition 6 is the midpoint where each isoform is predicted to be at 50%. Total amounts of transfected DNA were identical in all conditions. A, flow cytometry analysis of surface BST2 in HEK-293T cells transfected with conditions 1 to 11 of the above-mentioned converging gradient for HA-BST2 WT (red) and Myc-BST2 R136A (blue). Ratios of each isoform for all conditions are plotted as percentage of total BST2, as calculated in the examples described in Fig. S3. B, relative ILT7 activation from converging BST2 gradient. ILT7⁺ NFAT-GFP reporter cells were co-cultured for 18–24 h with control (empty) or HEK-293T cells expressing the above-mentioned BST2 gradient for 18–24 h and analyzed by flow cytometry. Percentage of ILT7 activation was plotted as % of GFP⁺ cells in each condition relative to the HA-BST2 WT condition (100%) after subtracting the % of GFP⁺ cells in the no BST2 condition (0%). The predicted curves if only homodimers of BST2 WT or if both homodimers of BST2 WT and heterodimers between BST2 WT and R136A were capable of activating ILT7 are indicated in dark gray squares and light gray triangles, respectively. The mean values of four independent experiments are plotted and error bars represent S.D.



Distinct domains of BST2 are involved in ILT7 activation

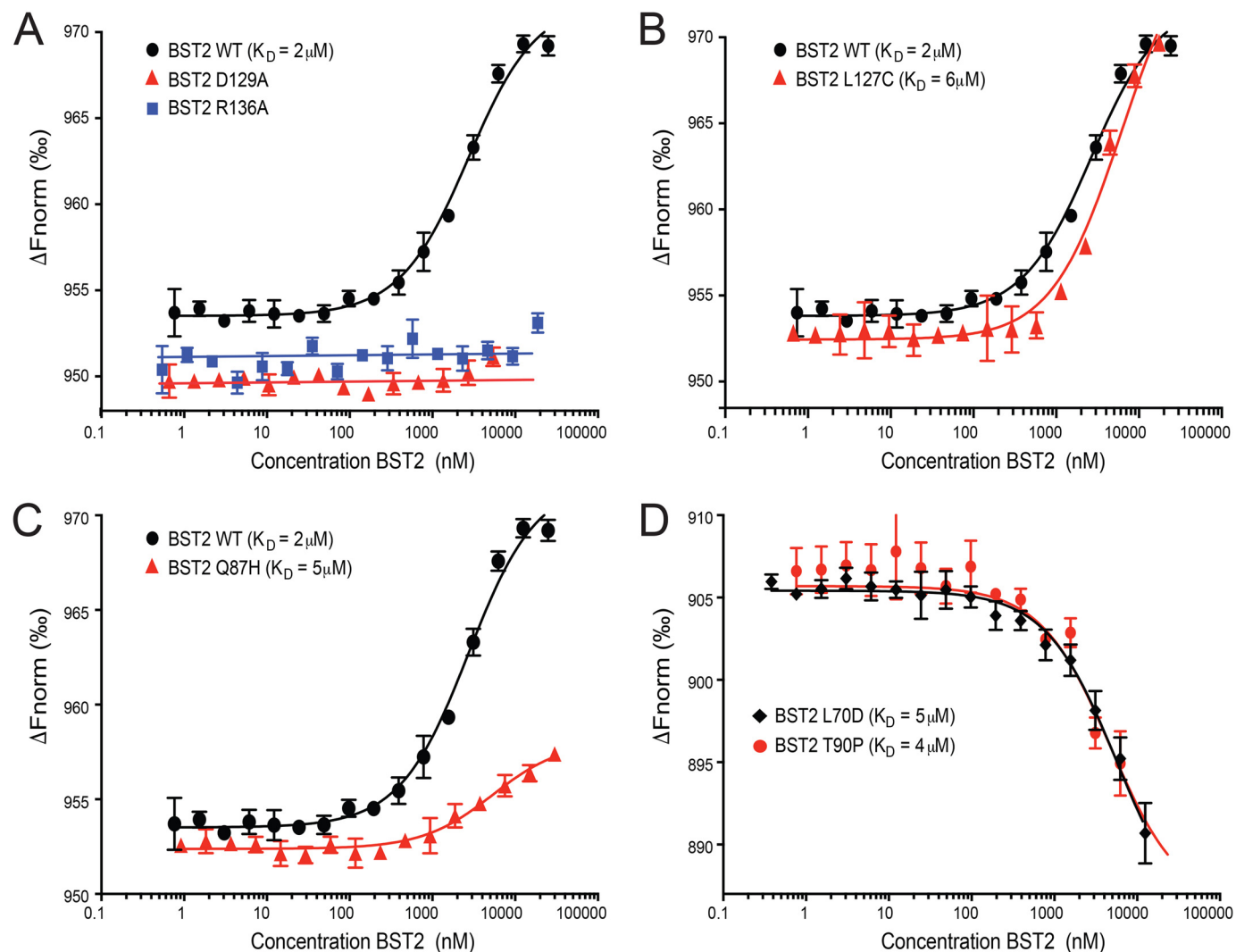


Figure 8. Thermophoretic analysis of BST2–ILT7 interaction. A series of 16 dilutions of recombinant BST2 (residues 47–159) WT or mutants were mixed with 1 μ M bacILT7(24–223). After 2 min incubation the samples were loaded into Monolith NT.115 Capillaries. Dose-response curve of ILT7 toward (A) BST2 WT or mutants D129A and R136A, (B) BST2 WT or mutant L127C, (C) BST2 WT or mutant Q87H, and (D) mutants L70D and T90P were generated. All experiments were done in triplicates. All resulting dose-response curves were fitted to a one-site binding model to obtain K_D values (indicated in graphs). Error bars indicate S.D. MST experiments were performed at a LED power of 80% and at medium MST power. *Fnorm*, normalized fluorescence.

Post-binding events associated to BST2 coiled-coil plasticity are required to activate ILT7

To further understand the molecular mechanism underlying ILT7 activation by BST2, we analyzed the binding strength of selected BST2 mutants to ILT7 using microscale thermophoresis (MST). The recorded binding strength of BST2 WT ectodomain to ILT7 ectodomain by MST (Fig. 8 and Fig. S4, $K_D = 2.45 \pm 0.3 \mu$ M) was remarkably similar to that as we previously reported using surface plasmon resonance (SPR) ($K_D = 2.33 \mu$ M (30)). Substitutions in the postulated ILT7-binding surface, BST2 D129A and R136A, that failed to activate ILT7 in the reporter assay and in the PBMC-based assay exhibited no bind-

ing to ILT7 by MST, validating these residues as critical for ILT7 binding (Fig. 8A and Fig. S4A). Interestingly, BST2 L127C mutant, which prevented BST2 activation of ILT7 in both functional assays by presumably limiting the plasticity of the coiled-coil, interacted with ILT7 with comparable strength than BST2 WT (Fig. 8B and Fig. S4B, $K_D = 6.45 \pm 1.2 \mu$ M), implying that binding to ILT7 is required but not sufficient to induce activation of the inhibitory receptor. MST analysis of BST2 mutants that enhanced ILT7 activation in the reporter assay (L70D, T90P, and Q87H) and in the PBMC assay (Q87H) revealed that none of these mutants displayed enhanced binding affinities. Indeed, these three mutants had K_D values in the lower micro-

Figure 7. Effect of natural variants of BST2 on ILT7 activation. A, relative BST2 surface expression in HEK-293T cells transfected with control plasmids or plasmids encoding the indicated BST2 mutants containing the SNPs or somatic mutations described in Table S1 ($n = 6$). All percentages of MFIs were calculated as described in the legend to Fig. 1. B, ILT7⁺ NFAT-GFP reporter cells were co-cultured for 18–24 h with HEK-293T cells expressing the indicated BST2 mutants and analyzed by flow cytometry ($n = 6$). Percentage of ILT7 activation was plotted as described in the legend to Fig. 1. Error bars represent S.D. C, control (Ctrl), BST2 WT, or selected mutants expressing HEK-293T cells were co-cultured with freshly isolated PBMCs and levels of bioactive IFN- γ released in supernatants in response to TLR7 agonist were measured as described in the legend to Fig. 3 ($n = 9$). Statistical significance was determined by applying repeated measures of ANOVA with Bonferroni's multiple comparison test.

molar range as BST2 WT, although with different thermophoresis (Fig. 8, C and D, and Fig. S4, C and D, Q87H $K_D = 5.06 \pm 1.1 \mu\text{M}$; L70D $K_D = 5.55 \pm 1 \mu\text{M}$; T90P $K_D = 4.49 \pm 0.9 \mu\text{M}$). Whereas BST2 WT and the BST2 Q87H mutant displayed a difference in amplitude when in complex with ILT7, BST2 mutants L70D and T90P showed a difference in signal direction. Chemical cross-linking of constructs comprising the recombinant ectodomain revealed that all mutants tested still dimerized as indicated by the appearance of new bands migrating at molecular masses between 25 and 35 kDa (Fig. S4E), as previously reported (26). To analyze the impact of the substitutions on the folding and stability of the proteins, we examined the circular dichroism (CD) profiles of selected BST2 mutants and determined their thermostability (melting temperature, T_m). CD analyses revealed that all mutants are highly α -helical in solution, with a propensity to form α helices either very similar to BST2 WT (Q87H, L127C) or just slightly reduced (70–90% helical content remaining for D129A, R136A, L70D, and T90P; Fig. S5, left panels). Analysis of the thermostability showed that whereas most mutants (D129A, L70D, Q87H, and T90P) displayed melting temperatures similar to BST2 WT ($\sim 61^\circ\text{C}$), mutants harboring substitutions at residues Leu-127 or Arg-136 in the coiled-coil domain exhibited a reduced thermostability with T_m values of ~ 53 and $\sim 54^\circ\text{C}$, respectively (Fig. S5, right panels). Despite the lower helical content and reduced thermostability of some of the mutants, none of them completely lost the integrity of the coiled-coil structure, as observed, for instance, under reducing conditions when the T_m drops to as low as $\sim 35^\circ\text{C}$ (26). Taken together, these results validate that post-binding events are governing the extent of ILT7 activation by BST2.

Discussion

The human BST2 coiled-coil is characterized by an inherent dynamic instability, which has been proposed to provide structural plasticity during dynamic events such as viral assembly and release (24–27). Indeed, the integrity of the coiled-coil structure rather than its amino acid sequence composition was found critical for optimal BST2 antiviral activity (22, 32, 33). However, the presence of large patches of amino acid sequence conservation between human BST2 and its counterparts encoded by other primates suggest that the structure could also be important for a conserved cellular function involving a cell-surface binding partner (27). A role of the BST2 coiled-coil as a binding interface for the ILT7 receptor is indeed supported by our *in vitro* binding studies revealing that this structure is sufficient for binding ILT7 as well as by our alanine scan mutagenesis, which clearly demonstrate that mutations encompassing the coiled-coil drastically affect ILT7 activation. Targeted mutagenesis of amino acid residues predicted to be exposed within the coiled-coil heptad repeats identify well-conserved residues Asp-129 and Arg-136 as essential on their own for binding ILT7 and as expected inducing its activation. We propose that these exposed residues in adjacent *c* positions represent the binding surface to ILT7. In the case of the aspartic acid residue at position 129, substitution for a similarly charged glutamic acid was found still detrimental for ILT7 activation, pointing to a critical role of an aspartic residue at that position.

Previous structural and functional studies have highlighted the critical role of disulfide linkages in stabilizing the BST2 dimer as well as the necessity for disulfide cross-linking through at least one of the three conserved cysteines for BST2 antiviral activity (21, 22, 24–27). The stabilizing role of disulfide bonds is also required for ILT7 activation. Disulfide cross-linking of cysteine 91 is predicted to prevent the detrimental effect of a neighboring asparagine residue on the BST2-mediated ILT7 activation. Interestingly, none of the other two cysteines, Cys-53 and Cys-63, were found to individually impact ILT7 activation, indicating that disulfide cross-linking at Cys-91 might serve two functions: first, ensuring the proper structural orientation of the C terminus of the ectodomain, and, second stabilizing the labile coiled-coil during dynamic processes of disassembly and reassembly, which confer a degree of conformational flexibility/plasticity to the molecule (23). Restricting the dynamic process of the BST2 coiled-coil with engineered disulfide bonds predicted to be formed at positions 127 and 134 drastically impaired ILT7 activation without, however, impairing binding of BST2 to the receptor (at least with L127C). These results suggest that whereas binding of BST2 to ILT7 is required for induction of ILT7 signaling, it might not be sufficient. This phenotype raises the possibility that post-binding events associated to the plasticity of the BST2 coiled-coil might be required for ILT7 activation, although we cannot entirely exclude that the lack of ILT7 activation might result from the slightly reduced thermostability of the L127C mutant.

Alanine scan and targeted mutagenesis of the N-terminal region of the BST2 ectodomain at amino acid residues 63, 70, 87, and 90 leads to an enhancement of ILT7 activation in the reporter assay without any major changes in the strength of binding to ILT7 (at least for the L70D, Q87H, and T90P mutants). These results suggest that this region of BST2 might exert a structural constraint on the ectodomain of the molecule. They also support the notion that besides binding, other molecular events might qualitatively impact BST2-mediated ILT7 activation. Disrupting a strong hydrophobic core close to the N terminus end of the dimer (L70D mutation) could provide more flexibility to the C terminus coiled-coil portion by reducing the backbone torsion downstream. Similarly, introducing a sharp helix break with a proline before the start of the coiled-coil region (T90P mutation), physically disconnecting the two domains, might relieve this structural constrain and favor ILT7 activation. Also, the presence of two membrane anchors restrains the ectodomain parallel to the plasma membrane. Therefore, some of the substitutions, such as L70D and E119K, may exert their effect by changing the electrostatic interactions with the negatively charged membrane.

On the basis of our analysis of the structure-function relationship of BST2 and the current literature, we propose the following model of BST2-mediated activation of the ILT7 pDC receptor. Two functionally active units of BST2 forming a stable dimer are required to activate ILT7. Upon binding of each BST2 molecule to a single monomeric ILT7/Fc ϵ RI γ pair at either side of the dimeric coiled-coil, the two ILT7/Fc ϵ RI γ pairs are brought close enough to induce their dimerization, a process that is facilitated by the conformational flexibility of the coiled-coil structure. Once close enough, a potential disulfide

Distinct domains of BST2 are involved in ILT7 activation

bond formation linking the two FcεRIγ co-receptors would stabilize the entire complex as observed for the Fc receptor complex (37). In this context, mutations D129A or R136A would prevent the initial binding, whereas mutation L127C would limit the conformational flexibility of the coiled-coil required to displace the ILT7/FcεRIγ complexes close enough for dimerization and subsequent signaling to occur. Relieving the structural constraint exerted by the N-terminal region of the BST2 ectodomain, as exemplified by L70D or T90P, would make this step more efficient by lowering the energy transition required to mediate this conformational rearrangement, thus allowing a more effective activation of the ILT7 receptor. Although this phenotype is observed in the reconstituted ILT7⁺ NFAT-GFP reporter cell assay (indicator cells are in a mouse hybridoma cell background), which might be more sensitive to structural changes that lower energy transitions, it was not detectable in the more physiological PBMC assay where formation of an active dimeric ILT7/FcεRIγ complex is likely more efficient and stable. Interestingly, a somatic mutation where glutamine 87 in the flexible connecting region was substituted with a histidine induced a significant increase of the ILT7 activation potential of BST2 in both assays, making it unlikely that this substitution caused this phenotype by lowering the energy transition of the predicted rearrangement step. Rather, the fact that the Q87H mutant binds ILT7 with an affinity comparable with BST2 WT suggests a potential role of the flexible connecting domain in modulating the quality of the BST2/ILT7 binding. Because the binding affinity of BST2 for the ILT7 receptor is rather low ($K_D \sim 2.5 \mu\text{M}$), clustering of BST2 of a higher order might be required to fully trigger the ILT7 signaling cascade. Small-angle X-ray scattering analysis of human and mouse BST2 revealed features indicative that the BST2 ectodomain can form higher order associations in solution (27). Accumulation of BST2 within the plasma membrane microdomain at the point of contact with pDC would support the formation of such high order associations and mutations facilitating or limiting the magnitude of this clustering might impact BST2-mediated ILT7 activation. Nevertheless, not all types of clusters would lead to a more effective activation of ILT7. For example, BST2 clusters at HIV-1–budding sites observed in cryo-EM studies in the absence of viral antagonist (38, 39) are unable to activate ILT7 most likely because of interference by entrapped virions (30). The same is true for antagonists that do not displace BST2 out of HIV-1–budding sites, such as the HIV-I group O Nef protein (31).

Elevated BST2 levels are observed in many types of malignant cells (15). The elevated BST2 mRNA levels observed in some metastatic and invasive tumors are a strong predictor of tumor size, aggressiveness, and often associated with poor patient survival (40, 41). Nonetheless, BST2 is not elevated in all cancer tissues as significant down-regulation was noted in particular cases, including B-cell acute lymphoblastic leukemia, liver, and prostate cancer (15, 42). Functional analyses of a selected number of BST2 ectodomain variants enriched in malignant cells when compared with healthy cells from the same individual reveal that most somatic mutations had no impact on BST2 activation except for two sequence variants, E119K and Q87H. The E119K variant found in melanoma abrogates ILT7 activa-

tion most likely by affecting the integrity of the coiled-coil structure. In contrast, the Q87H variant associated with colorectal cancer enhances the ILT7 activating capacity of BST2. Thus, these variants, although very rare, could confer evolutionary advantages to the malignant tumors they are associated with by enabling them to modulate pDC's IFN-I responses and hence either escape IFN-I anti-tumor activity (Q87H) or promote IFN-I pro-tumorigenic potential (E119K) (8, 43).

The IFN system can mount an early and extremely powerful antiviral and antitumor response. By modulating the immune response at its foundation, IFNs can widely reshape immunity to control chronic infectious diseases and invading malignancies. A better understanding of the intimate interplay between BST2 and ILT7 can open new avenues for targeted drug design in the context of antiviral or anti-cancer strategies.

Experimental procedures

Antibodies and reagents

Rabbit polyclonal anti-BST2 serum was previously described (44). Mouse monoclonal antibodies (mAb) anti-HA (HA.11 clone 16B12), and anti-ILT7_alexa647 were acquired from Biolegend. Rabbit anti-Myc Abs and Protein A-horseradish peroxidase were purchased from Sigma and Southern Biotech, respectively. All secondary Abs used for flow cytometry were purchased from Life Technologies. TLR7 agonists Gardiquimod (final concentration: $2.5 \mu\text{g/ml}$) was obtained from InvivoGen.

Cell lines and plasmids

HEK-293T and HEK-blue human IFN reporter cell lines were obtained from ATCC and InvivoGen, respectively. These cells were maintained in Dulbecco's modified Eagle's medium supplemented with 10% FBS. The ILT7 NFAT-GFP (CT550) cells were described previously (10). These cells were maintained in RPMI supplemented with 10% FBS. High Five insect cells were maintained at a cell density of $0.5\text{--}1 \times 10^6$ cells/ml in Express Five medium (Life Technologies) supplemented with 16 mM L-glutamine. HEK-293T cells were transiently transfected using Lipofectamine 2000 (Invitrogen). Usually, $0.5\text{--}1.5 \mu\text{g}$ of DNA was added to each well of a 24-well plate (125,000 cells/well) and medium was replaced 18–24 h post transfection. Unless specified otherwise, untagged BST2 open reading frames were cloned into the pcDNA3.1 backbone for transient transfections. Tagged versions of BST2 WT ORF (with internal tags added after amino acid 154) plus cloning restriction enzymes sites were chemically synthesized (Invitrogen) and cloned in the pcDNA3.1 backbone. All mutations introduced in BST2 were generated by PCR-based mutagenesis using specific primers (Table S2). All mutations were validated by automated sequencing. BST2 alanine scanning mutants (cloned in pFLAG-tetherin, with N-terminal tag) were a kind gift from Dr. Paul Spearman (32). Each mutant in the panel incorporates four alanine residues, starting from amino acid position 47 and continuing through to position 150.

Surface antigen staining and flow cytometry analysis

BST2 cell-surface staining and flow cytometry analysis was performed as previously described (44). Briefly, HEK-293T cells

were washed in PBS and stained with the specific primary antibody (anti-BST2 rabbit serum, anti-HA, or anti-Myc) for 45 min at 4 °C. Cells were then washed and stained using appropriate Alexa Fluor-coupled secondary Abs for 30 min at 4 °C. After an additional wash, cells were analyzed for cell-surface BST2 expression by flow cytometry. Cells from co-cultures between transfected HEK-293T and ILT7⁺ NFAT-GFP reporter cells were collected, washed in PBS, and stained with anti-ILT7_alexa647 antibodies for 45 min at 4 °C. Cells were then washed and analyzed for cell-surface ILT7 and GFP expression by flow cytometry. Fluorescence intensities were acquired using a Cyan ADP flow cytometer and data were analyzed using the FlowJo software (Treestar). In all histograms shown, mean fluorescence intensity (MFI) values are shown for each sample.

Activation of ILT7 using ILT7⁺ NFAT-GFP reporter cells

Two days prior to co-culture, HEK-293T cells were transfected with empty pcDNA3.1, and plasmids encoding for BST2 WT or mutants. ILT7⁺ NFAT-GFP reporter cells (100,000 cells/well) were added in a final volume of 500 μ l. The co-cultures were maintained for an additional 18–24 h, at which time samples were analyzed by flow cytometry for surface ILT7 and % of GFP expressing reporter cells from the ILT7⁺ gate. Given that the extent of ILT7 activation is directly proportional to surface levels of BST2 on co-cultured 293T targets cells (30), expression of all BST2 mutants was standardized to match that of the internal BST2 WT control.

Preparation of PBMCs and co-cultures

Peripheral blood samples were obtained from healthy adult donors who gave written informed consent in accordance with the Declaration of Helsinki under research protocols approved by the research ethics review board of the IRCM. PBMCs were isolated by Ficoll-Paque centrifugation (GE Healthcare) and cultured in RPMI 1640 medium supplemented with 10% FBS. Two days prior to co-culture, HEK-293T cells were transfected with empty pcDNA3.1 or plasmids encoding for BST2 WT or mutants. PBMCs at a ratio of 3:1 (PBMC:293T cell) were added in a final volume of 250 μ l. After 4 h of co-culture, TLR7 agonist Gardiquimod was added to a final concentration of 2.5 μ g/ml and cells were kept in co-culture for an additional 18–24 h as previously described (30). In all conditions, co-cultures were then transferred to a V-bottom 96-well plate and centrifuged for 5 min at 400 \times g. As a control, transfected HEK-293T cells were treated with TLR7 agonist in the absence of PBMCs. Supernatants were then used to quantify the amounts of bioactive IFN-I produced. Each experimental replicate (*n*) was performed using cells from a different donor.

Quantification of IFN-I

Detection of bioactive human IFN-I was performed using the reporter cell line HEK-Blue IFN- α/β (InvivoGen) as previously described (12). IFN-I concentration (units/ml) was extrapolated from the linear range of a standard curve generated using known amounts of IFN-I.

Surface plasma resonance

For SPR analysis, a synthetic codon-optimized ILT7 DNA fragment (*LILRA4*), encoding residues 24 to 435 (Eurofins Genomics) was cloned into the transfer vector pFL, followed by Tn7-based transposition into the EMBAcY bacmid to generate a recombinant baculovirus (bacILT7 24–435) (45). The extended coiled-coil domain of BST2 (residues 80 to 147) was cloned into the pBADM30 expression vector to construct a His-tagged GST fusion protein. The supernatant of SF21 insect cells secreting bacILT7 was collected 4 days post infection, dialyzed against buffer A (20 mM Tris, 150 mM NaCl, pH 7.2), and concentrated 2-fold. The supernatant was then applied to a nickel-affinity chromatography (Qiagen) column. The column was washed sequentially with buffer A containing 10, 50, and 70 mM imidazole, followed by elution of bacILT7 with buffer A containing 300 mM imidazole. The eluted fractions were pooled and dialyzed extensively against buffer B (20 mM Tris, 150 mM NaCl, 10% glycerol). Analytical size exclusion chromatography showed that the majority of the protein eluted in a peak at 13 ml from a Superdex 200 column (GE Healthcare). BacILT7 was dialyzed against HBS-PE and cleared by centrifugation at 100,000 \times g for 20 min. GST-BST2 (80–147) was expressed in *E. coli* Rosetta (DE3) cells (Novagen) and purified in buffer C (20 mM Tris, 100 mM NaCl, pH 7.5) by nickel-affinity chromatography (Qiagen) followed by size-exclusion chromatography on a Superdex 200 column in buffer D (20 mM HEPES, 100 mM NaCl, 10 mM EDTA, pH 7.5). SPR was performed on a Biacore 3000 (GE Healthcare) system using HBS-PE as a running buffer (10 mM HEPES, pH 7.5, 150 mM NaCl, 3 mM EDTA, and 0.005% Tween 20). GST-BST2(80–147) was diluted to 5 μ g/ml in 10 mM sodium acetate (pH 4) buffer and covalently immobilized to the surface of a CM5 sensor chip by amine coupling according to the manufacturer's instructions, yielding an R_{ligand} of 6550 RU. A reference flow cell was generated by amine coupling of GST alone ($R_{\text{ligand}} = 1028$). BacILT7 was serially diluted into running buffer and passed over the chip at a flow rate of 10 μ l/min. The response from the GST-coated reference cell was subtracted from the response resulting from specific binding to the target protein. Regeneration of the sensor chip was achieved with 10 mM HCl for 60 s. The spikes present in the sensorgrams are due to a delay in the bulk refractive index change between the flow cells, which is exacerbated by the 10 μ l/min flow rate. Data were analyzed with the BIAevaluation software version 4.1.

BST2 dimerization assay

A converging (or double) gradient of expression was generated by transfecting different ratios of plasmids encoding HA-BST2 WT and Myc-BST2 R136A mutants such that conditions 1 and 11 represent only HA-BST2 WT or Myc-BST2 R136A, respectively, and condition 6 is the midpoint where each plasmid was transfected at equal ratios (50% of each). For each condition, 1.2 μ g of total DNA was transfected. The ratio of each expression plasmid varied by 10% between each condition such that as the HA-BST2 WT-expressing plasmid was reduced, the Myc-BST2 R136A-expressing plasmid was increased. Forty-eight hours post transfection, a replica well was used for co-culture with ILT7⁺ NFAT-GFP reporter cells

Distinct domains of BST2 are involved in ILT7 activation

to measure ILT7 activation as described above. In parallel, another replica well was used for surface BST2 staining using anti-HA, anti-Myc, or anti-BST2 antibodies followed by flow cytometry analysis. Staining for total BST2 was used as an internal control to ensure that similar levels of total surface BST2 were achieved for all transfection conditions.

Co-immunoprecipitation and Western blotting

HA-CAML- or HA-BST2 WT-expressing plasmids were co-transfected with Myc-tagged BST2 (WT or R136A) expressors in HEK-293T. Cells were harvested and lysed in RIPA-DOC buffer (10 mM Tris, pH 7.2, 140 mM NaCl, 8 mM Na₂HPO₄, 2 mM NaH₂PO₄, 1% Nonidet P-40, 0.5% SDS, 1.2 mM deoxycholate) 48 h post-transfection. Ten percent of each lysate was preserved to control for protein expression (input). The remaining cell lysates were incubated with anti-HA for 2 h at 4 °C, prior to precipitation with Protein A-Sepharose beads (GE Healthcare). Immunoprecipitates were separated by 12.5% SDS-PAGE and analyzed for the presence HA-BST2 WT or Myc-BST2 (WT or R136A) or the negative control HA-CAML by Western blotting using either anti-HA or anti-Myc Abs.

Microscale thermophoresis

ILT7(24–223) was expressed and purified as indicated above. ILT7 eluting in the central fraction from the gel filtration column corresponding to monomeric ILT7 was used for all microscale thermophoresis experiments at 1.1 μ M in a buffer containing 20 mM HEPES, pH 7.5, 150 mM NaCl. The BST2 ectodomain (residues 47 to 159), WT or mutants, were cloned into expression vector pPROEX HTb (Invitrogen). BST2 protein expression was performed in *Escherichia coli* Rosetta2 cells induced with isopropyl 1-thio- β -D-galactopyranoside at 20 °C overnight. Cells were lysed in buffer A (20 mM Tris, pH 8.0, 100 mM NaCl, 10 mM imidazole). Proteins were purified by nickel-affinity chromatography, and washed with buffer B (20 mM Tris, pH 8.0, 100 mM NaCl) containing 20 and 50 mM imidazole for the first and second wash. Only one wash was performed for the BST2 L70D mutant purification. The bound protein fraction was eluted with buffer B containing 250 mM imidazole. The His tag was removed by tobacco etch virus protease cleavage and both tobacco etch virus and uncleaved protein were removed by nickel-affinity chromatography. Final purification steps included a size exclusion chromatography (Superdex 75, GE Healthcare) in buffer C (20 mM HEPES, pH 7.5, 150 mM NaCl). The supernatant of High Five insect cells secreting bacILT7 was collected 4 days post infection, dialyzed against buffer A (20 mM Tris, 150 mM NaCl, pH 7.2). The supernatant was then applied to a nickel-affinity chromatography (His Trap excel, GE Healthcare) equilibrated with buffer B (20 mM Tris, pH 7.2, 150 mM NaCl) and washed with buffer B containing 30 mM imidazole. The bound protein fraction was eluted with buffer B containing 500 mM imidazole and 10% glycerol. The final purification step included a size exclusion chromatography (Superdex 200 increase column, GE Healthcare) in buffer C (20 mM HEPES, pH 7.5, 150 mM NaCl). ILT7-purified protein was labeled using the Protein Labeling Kit RED-NHS (NanoTemper Technologies). The labeling reaction was performed according to the manufacturer's instructions. The labeled ILT7

was adjusted to 1 μ M with a buffer containing 20 mM HEPES, pH 7.5, 150 mM NaCl and supplemented with 0.05% Tween 20. A series of 16 1:1 dilutions of BST2 WT or mutants was prepared using the same buffer. For the measurement, each ligand dilution was mixed with 1 volume of labeled ILT7, and the samples were loaded into Monolith NT.115 Capillaries (NanoTemper Technologies). Instrument parameters were adjusted to 80% LED power and medium MST power (40%). Data of three independently pipetted measurements were analyzed (MO.Affinity Analysis software version 2.3, NanoTemper Technologies) using the signal from an MST-on time of 20 s.

Biophysical characterization of BST2 by circular dichroism (CD)

CD spectroscopy measurements were performed using a JASCO spectropolarimeter equipped with a thermoelectric temperature controller. Spectra of each sample were recorded at 20 °C in buffer A (50 mM phosphate, pH 7.5). For thermal denaturation experiments, the ellipticity was recorded at 222 nm with 1 °C steps from 20 to 92 °C with a slope of 1°/min. Ellipticity values were converted to mean residue ellipticity.

Cross-linking

BST2 WT and mutants were cross-linked with 5 mM EGS (ethylene glycol bis (succinimidylsuccinate), Pierce) at 1 mg/ml in a buffer containing 50 mM phosphate, pH 7.5, for 15 min at room temperature. Cross-linked samples were separated on a 15% SDS-PAGE and stained with Coomassie Brilliant Blue.

Statistical analysis

Statistical analysis was performed using repeated measures ANOVA, with Bonferroni's multiple comparison test or two-tailed paired Student's *t* tests. A *p* value of <0.05 was considered significant. The following symbols were used throughout the manuscript: ***, *p* < 0.001; **, *p* < 0.01; *, *p* < 0.05, *ns*, not significant (*p* > 0.05).

Author contributions—M. G. B. and E. A. C. conceptualization; M. G. B., N. M., A. L., N. A., and F. G. formal analysis; M. G. B., N. M., A. L., N. A., F. G., and A. A. M. investigation; M. G. B., N. M., A. L., N. A., F. G., and A. A. M. methodology; M. G. B. and E. A. C. writing-original draft; M. G. B., W. W., and E. A. C. writing-review and editing; W. W. and E. A. C. supervision.

Acknowledgments—We thank E. Massicotte and J. Lord-Grignon for assistance with flow cytometry; the IRCM clinic staff, and all volunteers for providing blood samples. The plasmids encoding the BST2 ectodomain with the nonoverlapping quadruple alanine mutations were a kind gift from Dr. Paul Spearman (University of Cincinnati). The ILT7 reporter cell lines were a generous gift from Dr. Y-J. Liu. We also thank Caroline Mas (ISBG, Biophysical Platform Manager) and Pierre Soule (Application specialist, Nanotemper society) for expert help with the analyses of the Microscale Thermophoresis experiments.

References

- Swiecki, M., and Colonna, M. (2015) The multifaceted biology of plasmacytoid dendritic cells. *Nat. Rev. Immunol.* **15**, 471–485 [CrossRef Medline](#)
- Essers, M. A., Offner, S., Blanco-Bose, W. E., Waibler, Z., Kalinke, U., Duchosal, M. A., and Trumpp, A. (2009) IFN α activates dormant haematopoietic stem cells *in vivo*. *Nature* **458**, 904–908 [CrossRef Medline](#)

3. Hwang, S. Y., Hertzog, P. J., Holland, K. A., Sumarsono, S. H., Tymms, M. J., Hamilton, J. A., Whitty, G., Bertoncello, I., and Kola, I. (1995) A null mutation in the gene encoding a type I interferon receptor component eliminates antiproliferative and antiviral responses to interferons α and β and alters macrophage responses. *Proc. Natl. Acad. Sci. U.S.A.* **92**, 11284–11288 [CrossRef Medline](#)
4. Swann, J. B., Hayakawa, Y., Zerafa, N., Sheehan, K. C., Scott, B., Schreiber, R. D., Hertzog, P., and Smyth, M. J. (2007) Type I IFN contributes to NK cell homeostasis, activation, and antitumor function. *J. Immunol.* **178**, 7540–7549 [CrossRef Medline](#)
5. Zitvogel, L., Galluzzi, L., Kepp, O., Smyth, M. J., and Kroemer, G. (2015) Type I interferons in anticancer immunity. *Nat. Rev. Immunol.* **15**, 405–414 [CrossRef Medline](#)
6. Chen, K., Liu, J., and Cao, X. (2017) Regulation of type I interferon signaling in immunity and inflammation: a comprehensive review. *J. Autoimmun.* **83**, 1–11 [CrossRef Medline](#)
7. Picard, C., and Belot, A. (2017) Does type-I interferon drive systemic autoimmunity? *Autoimmun. Rev.* **16**, 897–902 [CrossRef Medline](#)
8. Snell, L. M., McGaha, T. L., and Brooks, D. G. (2017) Type I interferon in chronic virus infection and cancer. *Trends Immunol.* **38**, 542–557 [CrossRef Medline](#)
9. Dzionek, A., Sohna, Y., Nagafune, J., Cella, M., Colonna, M., Facchetti, F., Günther, G., Johnston, I., Lanzavecchia, A., Nagasaka, T., Okada, T., Vermi, W., Winkels, G., Yamamoto, T., Zysk, M., Yamaguchi, Y., and Schmitz, J. (2001) BDCA-2, a novel plasmacytoid dendritic cell-specific type II C-type lectin, mediates antigen capture and is a potent inhibitor of interferon α/β induction. *J. Exp. Med.* **194**, 1823–1834 [CrossRef Medline](#)
10. Cao, W., Rosen, D. B., Ito, T., Bover, L., Bao, M., Watanabe, G., Yao, Z., Zhang, L., Lanier, L. L., and Liu, Y. J. (2006) Plasmacytoid dendritic cell-specific receptor ILT7-Fc ϵ RI γ inhibits Toll-like receptor-induced interferon production. *J. Exp. Med.* **203**, 1399–1405 [CrossRef Medline](#)
11. Cao, W., Bover, L., Cho, M., Wen, X., Hanabuchi, S., Bao, M., Rosen, D. B., Wang, Y. H., Shaw, J. L., Du, Q., Li, C., Arai, N., Yao, Z., Lanier, L. L., and Liu, Y. J. (2009) Regulation of TLR7/9 responses in plasmacytoid dendritic cells by BST2 and ILT7 receptor interaction. *J. Exp. Med.* **206**, 1603–1614 [CrossRef Medline](#)
12. Bego, M. G., Mercier, J., and Cohen, E. A. (2012) Virus-activated interferon regulatory factor 7 upregulates expression of the interferon-regulated BST2 gene independently of interferon signaling. *J. Virol.* **86**, 3513–3527 [CrossRef Medline](#)
13. Epeldegui, M., Blom, B., and Uittenbogaart, C. H. (2015) BST2/Tetherin is constitutively expressed on human thymocytes with the phenotype and function of Treg cells. *Eur. J. Immunol.* **45**, 728–737 [CrossRef Medline](#)
14. Cao, W., and Bover, L. (2010) Signaling and ligand interaction of ILT7: receptor-mediated regulatory mechanisms for plasmacytoid dendritic cells. *Immunol. Rev.* **234**, 163–176 [CrossRef Medline](#)
15. Mahauad-Fernandez, W. D., and Okeoma, C. M. (2016) The role of BST-2/tetherin in host protection and disease manifestation. *Immun. Inflamm. Dis.* **4**, 4–23 [CrossRef](#)
16. Kupzig, S., Korolchuk, V., Rollason, R., Sugden, A., Wilde, A., and Banting, G. (2003) Bst-2/HM1.24 is a raft-associated apical membrane protein with an unusual topology. *Traffic* **4**, 694–709 [CrossRef Medline](#)
17. Galao, R. P., Le Tortorec, A., Pickering, S., Kueck, T., and Neil, S. J. (2012) Innate sensing of HIV-1 assembly by tetherin induces NF κ B-dependent proinflammatory responses. *Cell Host Microbe* **12**, 633–644 [CrossRef Medline](#)
18. Rollason, R., Korolchuk, V., Hamilton, C., Schu, P., and Banting, G. (2007) Clathrin-mediated endocytosis of a lipid-raft-associated protein is mediated through a dual tyrosine motif. *J. Cell Sci.* **120**, 3850–3858 [CrossRef Medline](#)
19. Ishikawa, J., Kaisho, T., Tomizawa, H., Lee, B. O., Kobune, Y., Inazawa, J., Oritani, K., Itoh, M., Ochi, T., and Ishihara, K. (1995) Molecular cloning and chromosomal mapping of a bone marrow stromal cell surface gene, BST2, that may be involved in pre-B-cell growth. *Genomics* **26**, 527–534 [CrossRef Medline](#)
20. Ohtomo, T., Sugamata, Y., Ozaki, Y., Ono, K., Yoshimura, Y., Kawai, S., Koishihara, Y., Ozaki, S., Kosaka, M., Hirano, T., and Tsuchiya, M. (1999) Molecular cloning and characterization of a surface antigen preferentially overexpressed on multiple myeloma cells. *Biochem. Biophys. Res. Commun.* **258**, 583–591 [CrossRef Medline](#)
21. Andrew, A. J., Miyagi, E., Kao, S., and Strebel, K. (2009) The formation of cysteine-linked dimers of BST-2/tetherin is important for inhibition of HIV-1 virus release but not for sensitivity to Vpu. *Retrovirology* **6**, 80 [CrossRef Medline](#)
22. Perez-Caballero, D., Zang, T., Ebrahimi, A., McNatt, M. W., Gregory, D. A., Johnson, M. C., and Bieniasz, P. D. (2009) Tetherin inhibits HIV-1 release by directly tethering virions to cells. *Cell* **139**, 499–511 [CrossRef Medline](#)
23. Weissenhorn, W., Miguet, N., Aschman, N., Renesto, P., Usami, Y., and Gottlinger, H. G. (2012) Structural basis of tetherin function. *Curr. HIV Res.* **10**, 298–306 [CrossRef Medline](#)
24. Schubert, H. L., Zhai, Q., Sandrin, V., Eckert, D. M., Garcia-Maya, M., Saul, L., Sundquist, W. I., Steiner, R. A., and Hill, C. P. (2010) Structural and functional studies on the extracellular domain of BST2/tetherin in reduced and oxidized conformations. *Proc. Natl. Acad. Sci. U.S.A.* **107**, 17951–17956 [CrossRef Medline](#)
25. Yang, H., Wang, J., Jia, X., McNatt, M. W., Zang, T., Pan, B., Meng, W., Wang, H. W., Bieniasz, P. D., and Xiong, Y. (2010) Structural insight into the mechanisms of enveloped virus tethering by tetherin. *Proc. Natl. Acad. Sci. U.S.A.* **107**, 18428–18432 [CrossRef Medline](#)
26. Hinz, A., Miguet, N., Natrajan, G., Usami, Y., Yamanaka, H., Renesto, P., Hartlieb, B., McCarthy, A. A., Simorre, J. P., Gottlinger, H., and Weissenhorn, W. (2010) Structural basis of HIV-1 tethering to membranes by the BST-2/tetherin ectodomain. *Cell Host Microbe* **7**, 314–323 [CrossRef Medline](#)
27. Swiecki, M., Scheaffer, S. M., Allaire, M., Fremont, D. H., Colonna, M., and Brett, T. J. (2011) Structural and biophysical analysis of BST-2/tetherin ectodomains reveals an evolutionary conserved design to inhibit virus release. *J. Biol. Chem.* **286**, 2987–2997 [CrossRef Medline](#)
28. Neil, S. J., Zang, T., and Bieniasz, P. D. (2008) Tetherin inhibits retrovirus release and is antagonized by HIV-1 Vpu. *Nature* **451**, 425–430 [CrossRef Medline](#)
29. Van Damme, N., Goff, D., Katsura, C., Jorgenson, R. L., Mitchell, R., Johnson, M. C., Stephens, E. B., and Guatelli, J. (2008) The interferon-induced protein BST-2 restricts HIV-1 release and is downregulated from the cell surface by the viral Vpu protein. *Cell Host Microbe* **3**, 245–252 [CrossRef Medline](#)
30. Bego, M. G., Côté, É., Aschman, N., Mercier, J., Weissenhorn, W., and Cohen, É. A. (2015) Vpu exploits the cross-talk between BST2 and the ILT7 receptor to suppress anti-HIV-1 responses by plasmacytoid dendritic cells. *PLoS Pathog.* **11**, e1005024 [CrossRef Medline](#)
31. Bego, M. G., Cong, L., Mack, K., Kirchhoff, F., and Cohen, É. A. (2016) Differential control of BST2 restriction and plasmacytoid dendritic cell antiviral response by antagonists encoded by HIV-1 group M and O strains. *J. Virol.* **90**, 10236–10246 [CrossRef Medline](#)
32. Hammonds, J., Ding, L., Chu, H., Geller, K., Robbins, A., Wang, J. J., Yi, H., and Spearman, P. (2012) The tetherin/BST-2 coiled-coil ectodomain mediates plasma membrane microdomain localization and restriction of particle release. *J. Virol.* **86**, 2259–2272 [CrossRef Medline](#)
33. Andrew, A. J., Berndsen, C. E., Kao, S., and Strebel, K. (2012) The size and conservation of a coiled-coil structure in the ectodomain of human BST-2/tetherin is dispensable for inhibition of HIV-1 virion release. *J. Biol. Chem.* **287**, 44278–44288 [CrossRef Medline](#)
34. Lepelletier, A., Louis, S., Sourisseau, M., Law, H. K., Pothlichet, J., Schilte, C., Chaperot, L., Plumas, J., Randall, R. E., Si-Tahar, M., Mammano, F., Albert, M. L., and Schwartz, O. (2011) Innate sensing of HIV-infected cells. *PLoS Pathog.* **7**, e1001284 [CrossRef Medline](#)
35. Crick, F. H. C. (1953) The packing of α -helices: simple coiled-coils. *Acta Crystallogr.* **6**, 689–697 [CrossRef](#)
36. McLachlan, A. D., and Stewart, M. (1975) Tropomyosin coiled-coil interactions: evidence for an unstaggered structure. *J. Mol. Biol.* **98**, 293–304 [CrossRef Medline](#)
37. Kuster, H., Zhang, L., Brini, A. T., MacGlashan, D. W., and Kinet, J. P. (1992) The gene and cDNA for the human high affinity immunoglobulin E receptor β chain and expression of the complete human receptor. *J. Biol. Chem.* **267**, 12782–12787 [Medline](#)

Distinct domains of BST2 are involved in ILT7 activation

38. Hammonds, J., Wang, J. J., Yi, H., and Spearman, P. (2010) Immuno-electron microscopic evidence for tetherin/BST2 as the physical bridge between HIV-1 virions and the plasma membrane. *PLoS Pathog.* **6**, e1000749 [CrossRef Medline](#)
39. Habermann, A., Krijnse-Locker, J., Oberwinkler, H., Eckhardt, M., Homann, S., Andrew, A., Strebel, K., and Kräusslich, H. G. (2010) CD317/tetherin is enriched in the HIV-1 envelope and downregulated from the plasma membrane upon virus infection. *J. Virol.* **84**, 4646–4658 [CrossRef Medline](#)
40. Mahaud-Fernandez, W. D., DeMali, K. A., Olivier, A. K., and Okeoma, C. M. (2014) Bone marrow stromal antigen 2 expressed in cancer cells promotes mammary tumor growth and metastasis. *Breast Cancer Res.* **16**, 493 [CrossRef Medline](#)
41. Mukai, S., Oue, N., Oshima, T., Mukai, R., Tatsumoto, Y., Sakamoto, N., Sentani, K., Tanabe, K., Egi, H., Hinoi, T., Ohdan, H., and Yasui, W. (2017) Overexpression of transmembrane protein BST2 is associated with poor survival of patients with esophageal, gastric, or colorectal cancer. *Ann. Surg. Oncol.* **24**, 594–602 [CrossRef Medline](#)
42. Gong, S., Osei, E. S., Kaplan, D., Chen, Y. H., and Meyerson, H. (2015) CD317 is over-expressed in B-cell chronic lymphocytic leukemia, but not B-cell acute lymphoblastic leukemia. *Int. J. Clin. Exp. Pathol.* **8**, 1613–1621 [Medline](#)
43. Di Franco, S., Turdo, A., Todaro, M., and Stassi, G. (2017) Role of type I and II interferons in colorectal cancer and melanoma. *Front. Immunol.* **8**, 878 [CrossRef Medline](#)
44. Dubé, M., Roy, B. B., Guiot-Guillain, P., Binette, J., Mercier, J., Chiasson, A., and Cohen, E. A. (2010) Antagonism of tetherin restriction of HIV-1 release by Vpu involves binding and sequestration of the restriction factor in a perinuclear compartment. *PLoS Pathog.* **6**, e1000856 [CrossRef Medline](#)
45. Trowitzsch, S., Bieniossek, C., Nie, Y., Garzoni, F., and Berger, I. (2010) New baculovirus expression tools for recombinant protein complex production. *J. Struct. Biol.* **172**, 45–54 [CrossRef Medline](#)
46. Rose, A. S., Bradley, A. R., Valasatava, Y., Duarte, J. M., Prlic, A., and Rose, P. W. (2018) NGL viewer: web-based molecular graphics for large complexes. *Bioinformatics* **34**, 3755–3758 [CrossRef Medline](#)